Fiber optic Bragg grating sensors for thermographic detection of subsurface anomalies

Sidney G. Allison, William P. Winfree and Meng-Chou Wu

NASA, Langley Research Center, MS 231, Hampton, Virginia, USA, 23681-2199

ABSTRACT

Conventional thermography with an infrared imager has been shown to be an extremely viable technique for nondestructively detecting subsurface anomalies such as thickness variations due to corrosion. A recently developed technique using fiber optic sensors to measure temperature holds potential for performing similar inspections without requiring an infrared imager. The structure is heated using a heat source such as a quartz lamp with fiber Bragg grating (FBG) sensors at the surface of the structure to detect temperature. Investigated structures include a stainless steel plate with thickness variations simulated by small platelets attached to the back side using thermal grease. A relationship is shown between the FBG sensor thermal response and variations in material thickness. For comparison, finite element modeling was performed and found to agree closely with the fiber optic thermography results. This technique shows potential for applications where FBG sensors are already bonded to structures for Integrated Vehicle Health Monitoring (IVHM) strain measurements and can serve dual-use by also performing thermographic detection of subsurface anomalies.

Keywords: fiber Bragg gratings, temperature sensors, integrated vehicle health monitoring, thermography

1. INTRODUCTION

Optical FBG sensors can be used to measure strain and other parameters such as temperature in numerous applications[1-9]. Distributed FBG sensing is particularly beneficial for Structural Health Monitoring (SHM) applications such as IVHM of aerospace vehicles. Numerous references to fiber grating developmental work can be found in a review of fiber grating sensors by Kersey et al.[10] A low reflectivity grating-based system[6] developed at NASA Langley Research Center (LaRC) is ideal for spaceflight because it has the ability to multiplex up to thousands of Bragg gratings in a single fiber.[9] The system is based on the principle of Optical Frequency Domain Reflectometry (OFDR)[5] and offers the advantage that all of the gratings are of nominally the same wavelength. Writing gratings at the same wavelength greatly simplifies manufacturing of the sensing fiber. Typical Bragg grating readout systems require gratings with much higher reflectivities. However, the OFDR employs a coherent detection scheme and is capable of reading out very low reflectivity gratings. This allows the recording and analysis of strain or temperature from a large number of gratings in a single fiber.

Prior applications have demonstrated use of fiber optic sensors to measure strain at ambient temperatures[3] as well as at low temperatures such as in cryogenic fuel tanks[11] in aerospace vehicles. Fiber optic sensors would be particularly advantageous in cryogenic fuel tanks because they would not pose an electrical arcing ignition source as failed strain gauges or other electronic sensors might. In addition, OFDR technology offers considerable weight savings since it can provide a large number of strain measurements per fiber whereas each conventional strain gauge requires individual electrical wiring. This paper examines potential for FBG sensors, in applications where already bonded to structures for IVHM strain measurements, to serve dual-use by also performing thermographic detection of subsurface anomalies.

Conventional thermographic techniques in general utilize a flash or quartz lamp as a heating source and an infrared imager to detect the thermal response of the investigated material. The heating pulse duration typically ranges from a fraction of a second to a few seconds. An IR imager contains an array of several hundred by hundred detectors. These techniques are capable of large area inspection of aerospace structures and materials for their reliability and safety. One

of the particularly important areas where conventional thermographic technique is applicable is the inspection of metallic plate/sheet materials because of their widespread use. Of particular interest in this paper is the detection of subsurface anomalies such as thickness variations resulting from corrosion.

Previous work proposed a new technique[12] using a single optical fiber with multiple FBG's for the thermographic detection of flaws on materials and structures. Wu et al demonstrated the new technique on a composite plate with built-in delaminations. This paper demonstrates the new technique on a 0.127 cm thick 321 stainless steel plate sample with thickness variations representative of corrosion simulated by 0.229 cm thick 321 stainless steel platelets bonded to the surface using thermal grease. Both during and following the application of a thermal heat flux to the surface, the individual Bragg grating sensors measured the temporal and spatial temperature variations. The data obtained from individual FBG's was compared to thermal finite element modeling results.

2. THEORETICAL RESPONSES

2.1 Relationship of change in Bragg grating wavelength to change in temperature

In general a fiber Bragg grating can be characterized by its Bragg wavelength, which is the center wavelength of the light reflected from the grating. The Bragg wavelength is given as

$$\lambda_B = 2n_{eff}\Lambda, \tag{1}$$

where n_{eff} is the effective refractive index of the fiber core and Λ the grating period. For a fiber Bragg grating bonded to a metallic substrate, a change in the temperature causes a change in the grating period due to not only the thermal expansion of the fiber but also the strain induced by thermal expansion of the substrate. In addition, the refractive index of the fiber core changes because of the thermo-optic effect. Combining all the above effects, the shift in the Bragg wavelength due to a temperature change, ΔT, is given as

$$\delta\lambda_B / \lambda_B = (1 - p_e)\delta l /l + \delta n_{eff} /n_{eff}, \tag{2}$$

where p_e is the photoelastic constant of the optical fiber and $\delta l /l$ is the thermally induced strain of the fiber. In general the photoelastic constant, the fractional index change, and the thermal expansion coefficients of the fiber and the substrate are temperature dependent and nonlinear, especially at low temperatures. However, for a finite temperature change, especially for the temperatures around and above the room temperature, Eq. (2) can be rewritten as a linear form as,[13]

$$\delta\lambda_B / \lambda_B = [(1 - p_e) \alpha_p + \xi]\Delta T, \tag{3}$$

where $\xi = (1/n_{eff})(\partial n_{eff} / \partial T)$, is the thermo-optic coefficient of the fiber and α_p is the thermal expansion coefficient of the substrate. Eq. (3) takes into account the conditions when the thermal expansion coefficient and the physical dimension of the substrate are much greater than those of the optical fiber. This simple equation allows the FBG to perform as a temperature sensor of the substrate.

2.2 One dimensional model of thermal response of flat plate

The thermal response for a flat plate with the two sides bounded at x=0 and x=l, an initial temperature of zero and a prescribed flux of F applied at $x=l$ and $t=0$ is given by[14]

$$T(x,t) = \frac{\varepsilon F}{\rho c l}t + \varepsilon F l /K \left\{ \frac{3x^2 - l^2}{6l^2} - \frac{2}{\pi^2}\sum_{n=1}^{\infty}\frac{-1^n}{n^2}e^{-\alpha n^2 \pi^2 t /l^2}\cos\left(\frac{n\pi x}{l}\right)\right\} \tag{4},$$

where ε is the surface emissivity, c is the specific heat and ρ is the density, K is the thermal conductivity of the plate and α is the thermal diffusivity. The terms in the sum represent the initial transient that occurs immediately after the heat is

applied to the surface. For times greater than or equal to l^2/α, the sum is approximately zero. For steel, the thermal diffusivity is 0.14 cm^2/sec, therefore for the case of the combined thicknesses of the plate and the platelet of 0.36 cm, all of the transients in the solution have disappeared within 0.9 seconds. The temperature at the heated surface is given by

$$T(l,t) = \frac{\varepsilon F}{\rho c l} t + \frac{\varepsilon F l}{3K} \tag{5},$$

and the temperature of the unheated surface is given by

$$T(0,t) = \frac{\varepsilon F}{\rho c l} t - \frac{\varepsilon F l}{6K} \tag{6}.$$

The rate of temperature change at the heated and non-heated surfaces are equal and inversely proportional to the thickness of the plate, if the flux and emissivities of the flux are the same.

3. EXPERIMENTAL DESIGN

3.1 Steel plate test sample

The test sample consists of a 35.5 cm x 35.5 cm x 0.127 cm 321 stainless steel plate as shown in the photographs in Fig. 1. The plate's front surface was spray painted flat black while the back surface was left unpainted. A Sharpy marker was used to draw a 5.08 cm x 5.08 cm grid over the 30.5 cm x 30.5 cm central portion of the sample and also to draw a finer 2.54 cm x 2.54 cm grid at the 15.2 cm x 15.2 cm central segment of the plate. These grid lines were marked on the front as well as on the back side to facilitate accurate attachment of measurement fiber on the front surface and heat sink platelets on the back side as will be discussed in the next paragraph.

In this study, an optical fiber with 29 FBGs equally spaced 5.08 cm apart was bonded to the 15.2 cm x 15.2 cm central segment of the front surface of the 321 stainless steel plate test specimen using Capton® tape, as shown in Fig. 1(a-c). This bonding technique allowed the optical fiber to be bonded and removed quickly and neatly, while providing sufficient bonding of the fiber to the substrate for the test conditions. Since the Bragg grating sensors in the fiber were spaced 5.08 cm apart whereas the measurement area grid used 2.54 cm x 2.54 cm squares, the fiber was first run in one direction to place a grating in the middle of every other square. The fiber was then doubled back so that a grating could be placed in the alternate squares of the measurement grid. The fiber then looped over to the next row of squares and the process was repeated. Each Bragg grating sensor had an active gauge length of 5 mm. The four 321 stainless steel heat sink platelets used for this testing each measured 2.54 cm x 2.54 cm x 0.229 cm and were bonded to the back of the test article as shown in Fig. 1(d) using thermal grease. Platelets were not painted and were positioned relatively far apart to minimize thermal cross talk.

3.2 Optical fiber with Bragg grating sensors

The single-mode optical fiber used in this experiment was drawn using the fiber optic draw tower at LaRC using a preform similar to that for making SMF 28 fiber, but having higher germanium doping. This resulted in fiber having higher numerical aperture and exhibiting lower bend loss than SMF 28 fiber would possess. The fiber contained Bragg gratings written at 1550.2 nm during the draw with an estimated low reflectivity of 0.004%. Typical Bragg grating measurement systems require gratings with much higher reflectivities. Low reflectivity Bragg gratings were used in this experiment because the OFDR system employs a coherent detection scheme and is designed with a high spatial resolution for reading multiple equal wavelength gratings with very low reflectivity. In fact, the OFDR can read hundreds of low-reflectivity gratings in a single fiber.
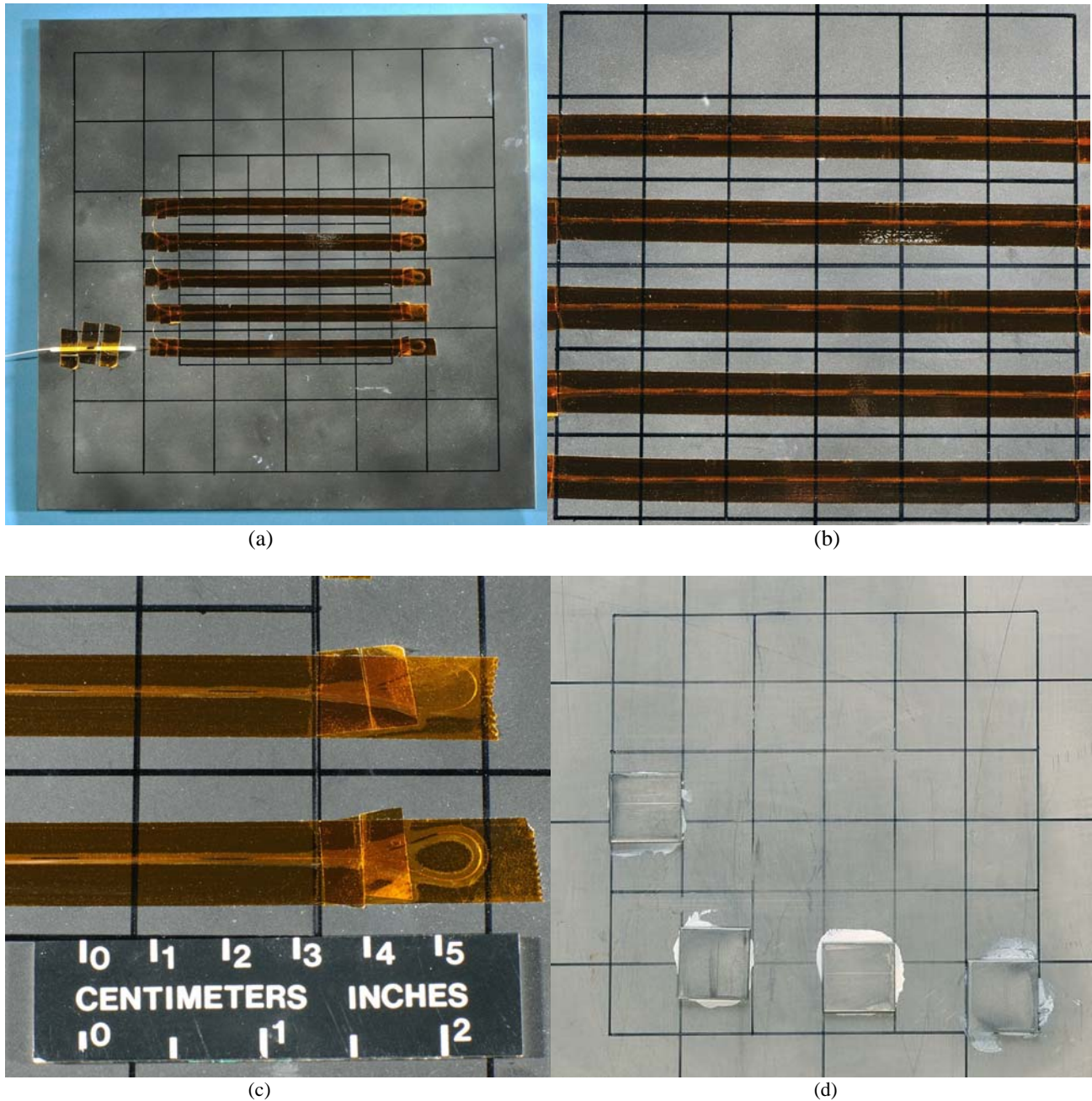
Figure 1. Photographs of the 35.5 cm x 35.5 cm x 0.127 cm 321 stainless steel plate test sample used for this research. The front of the plate was spray painted flat black. (a-b) Gage area 15.2 cm x 15.2 cm in the center of the plate's front surface has optical measurement fiber taped on. (c) Close up view of optical sensing fiber taped to test article. (d) Back of the test sample was not painted and has unpainted 321 stainless steel platelets 2.54 cm x 2.54 cm x 0.229 cm attached using thermal grease. Platelets were positioned relatively far apart to minimize thermal cross talk.

As the fiber was drawn, gratings were written 5.08 cm apart on the bare fiber as it emerged from the preform melt furnace of the draw tower. As the fiber with gratings continued moving down the draw tower, it was coated with two layers of polyimide cured by infrared ovens before the finished fiber was spooled and ready for use. The finished fiber had a 0.152 mm overall diameter including the coating. The role of the coating is to protect the fiber.[15-16] Bare or uncoated fibers are exceedingly weak due to the ease of extrinsic flaw formation by surface abrasion and attack from

moisture and other hostile chemicals in the environment. A patch cord was fusion spliced to one end of the measurement fiber for connecting to the OFDR system. A fusion splice protector reinforced the splice region and was taped to the sample surface as seen in Fig. 1(a-b).

3.3 Fiber and heat sink platelet layout

Fig. 2 is a schematic of the test area in the middle section of the plate showing locations of FBG"s and platelets. Although the fiber contains a total of 29 FBG's, for this study only the thirteen FBG's of interest were labeled for simplicity. Note that FBG1 is 0 cm away from the centerline of its nearest platelet, FBG2 is 0.635 cm away from its nearest platelet, etc. Heat sink platelets were lapped to assure flatness before being bonded to the back surface using thermal grease.
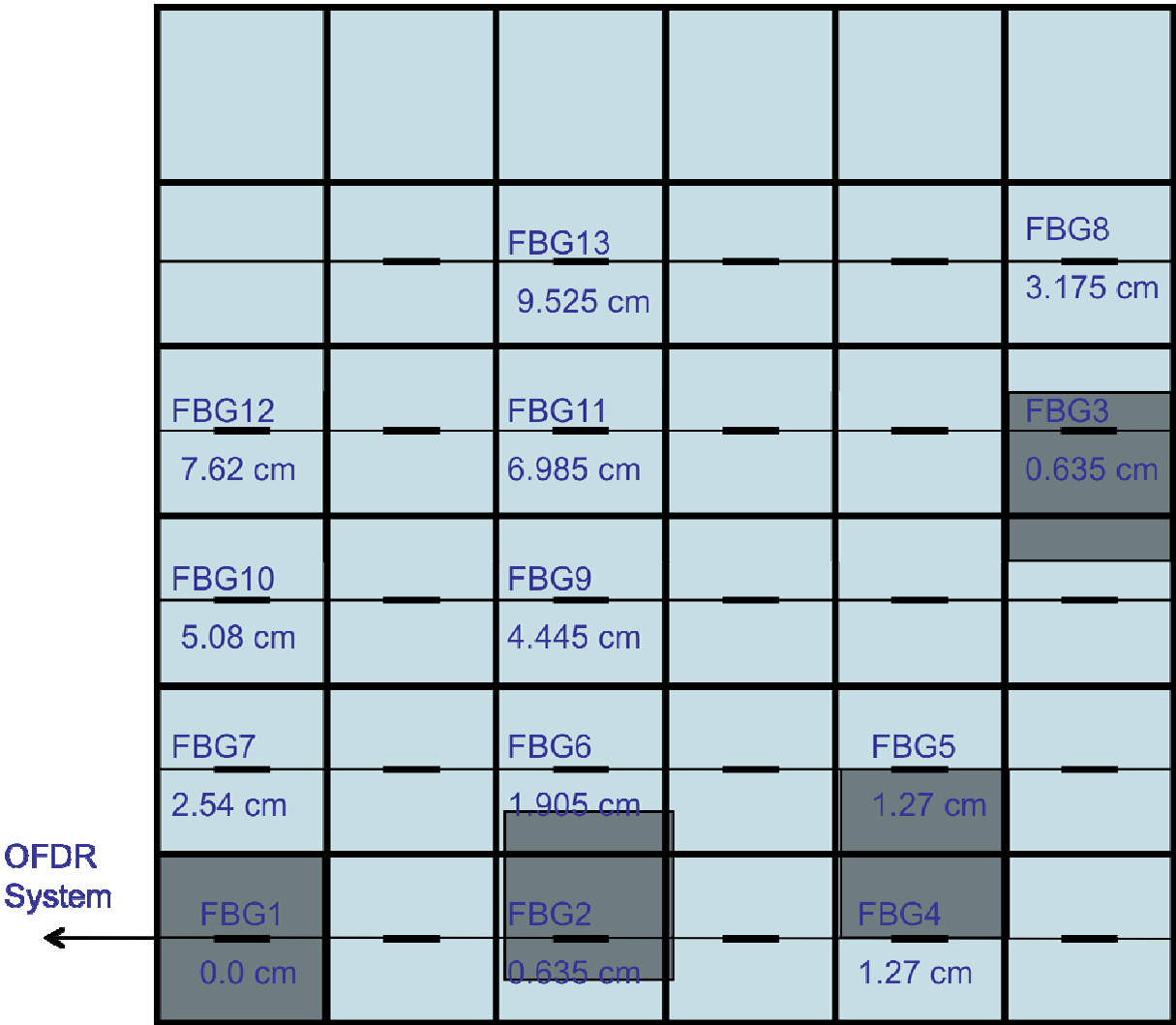

Figure 2. Schematic of 15.2 cm x 15.2 cm test area in the central section of the plate seen in Fig. 1(a-b) showing locations of FBG sensors and heat sink platelets. For simplicity only the thirteen FBG's of interest are labeled. FBG1 is 0 cm away from the centerline of its nearest platelet, FBG2 is 0.635 cm away from its nearest platelet, etc.

3.4 Test setup and procedure

The experimental setup is shown in Fig. 3. The OFDR fiber optic distributed sensing system had one data acquisition channel. A quartz lamp was used to heat the front and back surfaces of the specimen. Heating duration was 20 seconds. Grating data acquisition was performed at a rate of about 2.85 Hz during and after the application of the heat flux to the surface. For these tests the OFDR measurement system started taking data a few seconds before the lamp was turned on and continued measuring during heating and for a period of time after the lamp was turned off.
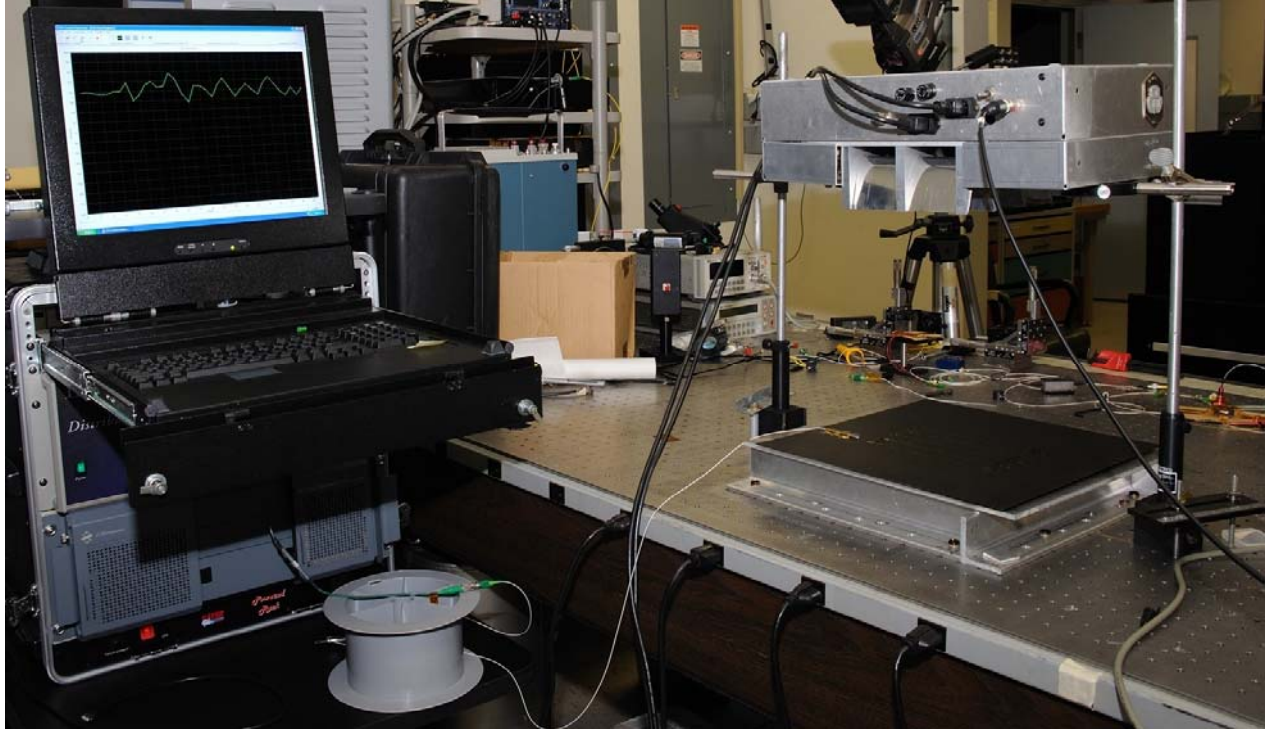
Figure 3. Photograph of test setup. The OFDR fiber optic distributed sensing system seen on the left had one data acquisition channel. The test article and Quartz lamp are on the optical table to the right. The test article was heated with the Quartz heat lamp for 20 seconds. Data was taken before, during and after heating.

4. MEASUREMENT RESULTS

Fig. 4 shows the front surface heating measurement temperature readings as a function of time for five of the FBG sensors. As can be seen from the figure, the sensors that are on or near to the platelet region (gratings 1,2 and 4) show a marked reduction in the rate of temperature heating with the quartz lamps on. This is attributed to the larger thermal mass in these regions as a result of the presence of the platelet on the backside of the specimen. After the end of heating, these regions tend to continue to increase in temperature as the heat flows from warmer regions around the platelet, into the platelet region. Fig. 5 shows a similar trend occurs with back surface (through transmission) heating measurement temperature readings as a function of time for the same five FBG sensors as shown in Fig. 4.

As can be seen in Eq. 5 and Eq. 6, after an initial transient response following the application of heat, the temperature of the plate should increase linearly with time at a rate that is inversely proportional the thickness of the plate. The linear response is seen in Fig. 4 from 11 sec to 31 sec and from 16 sec to 36 sec in Fig. 5. To find the slope of these responses, a least-squares linear fit was performed. Some of the typical fits are shown in Fig. 6. As can be seen, the fits are well within the noise of the data. Fig. 7 shows slope parameter of the temperature fits vs. FBG distance from platelets.
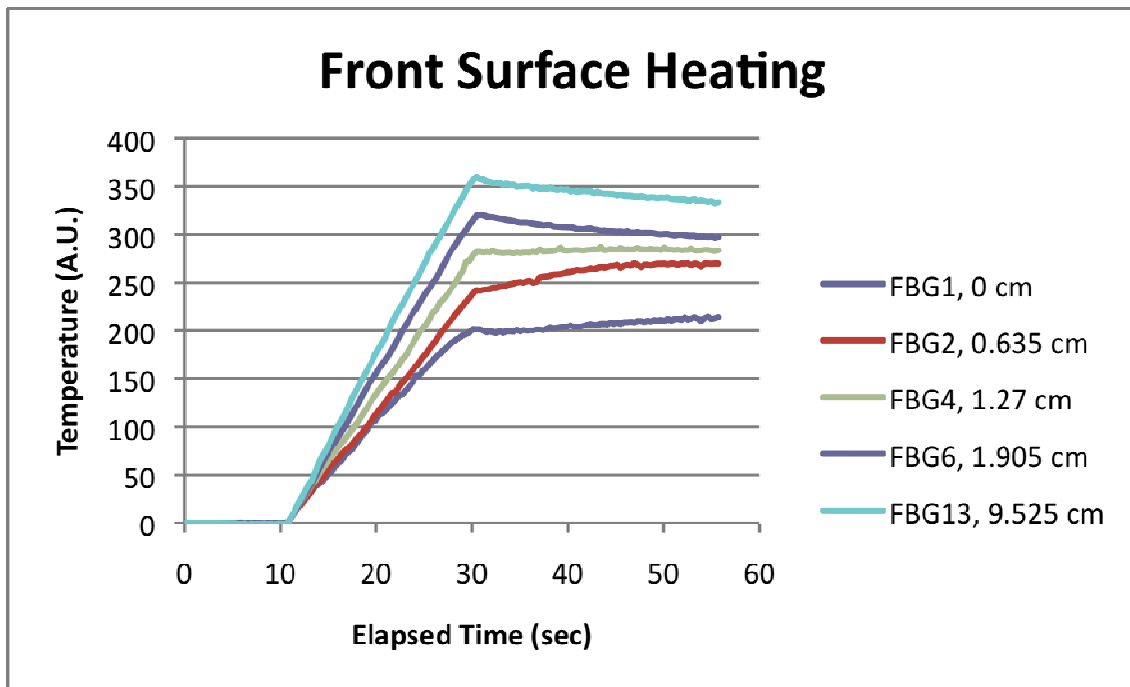
Figure 4. Measured front surface heating temperature as a function of time for five of the FBG sensors located different distances from the nearest heat sink platelets.
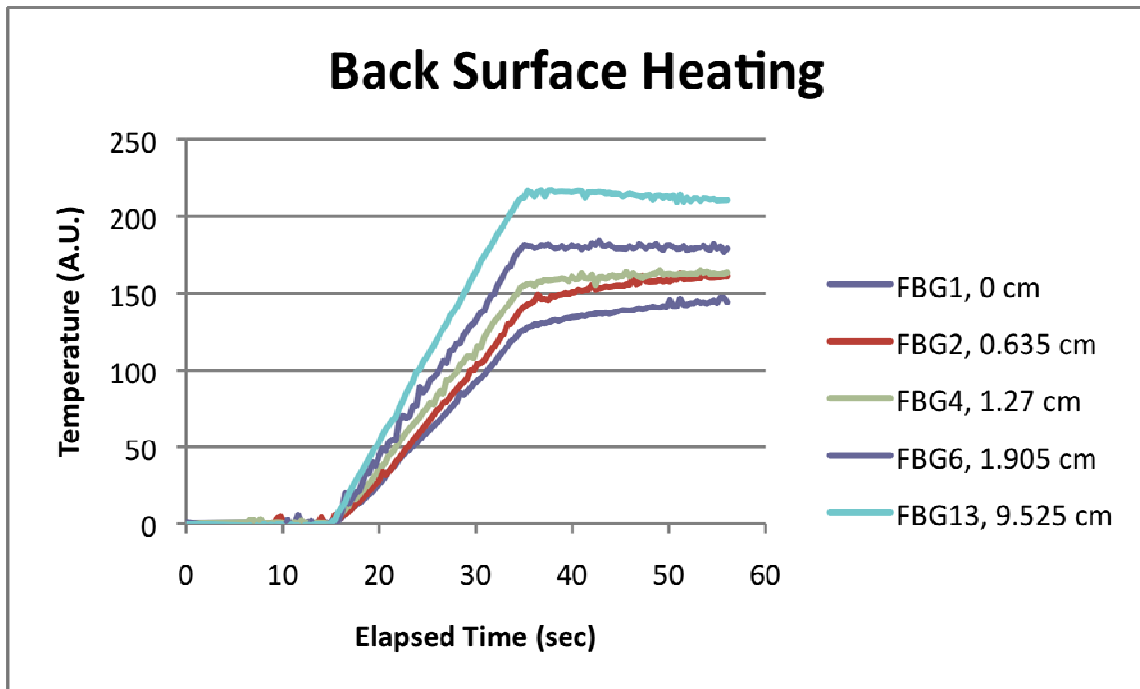

Figure 5. Measured back surface (through transmission) heating temperature as a function of time for the same five FBG sensors shown in Fig. 4.
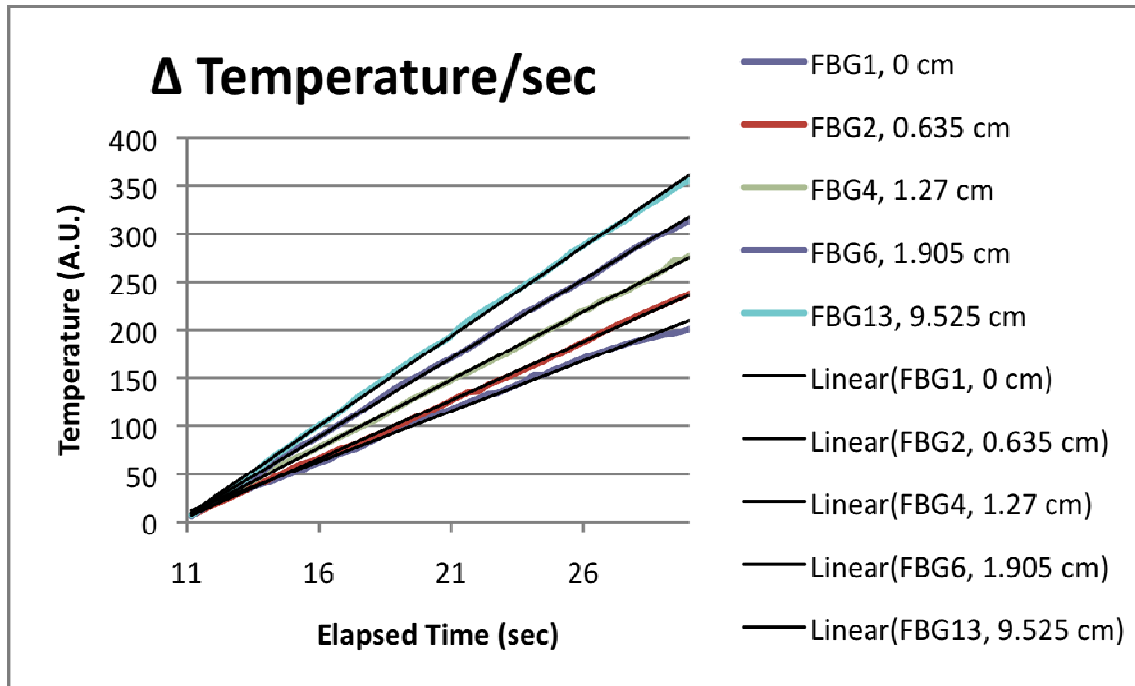
Figure 6. Typical temperature measured as a function of time during sample heat-up for several FBG sensors. Linear least-squares fits of the temperature are superimposed over measured values with excellent agreement.
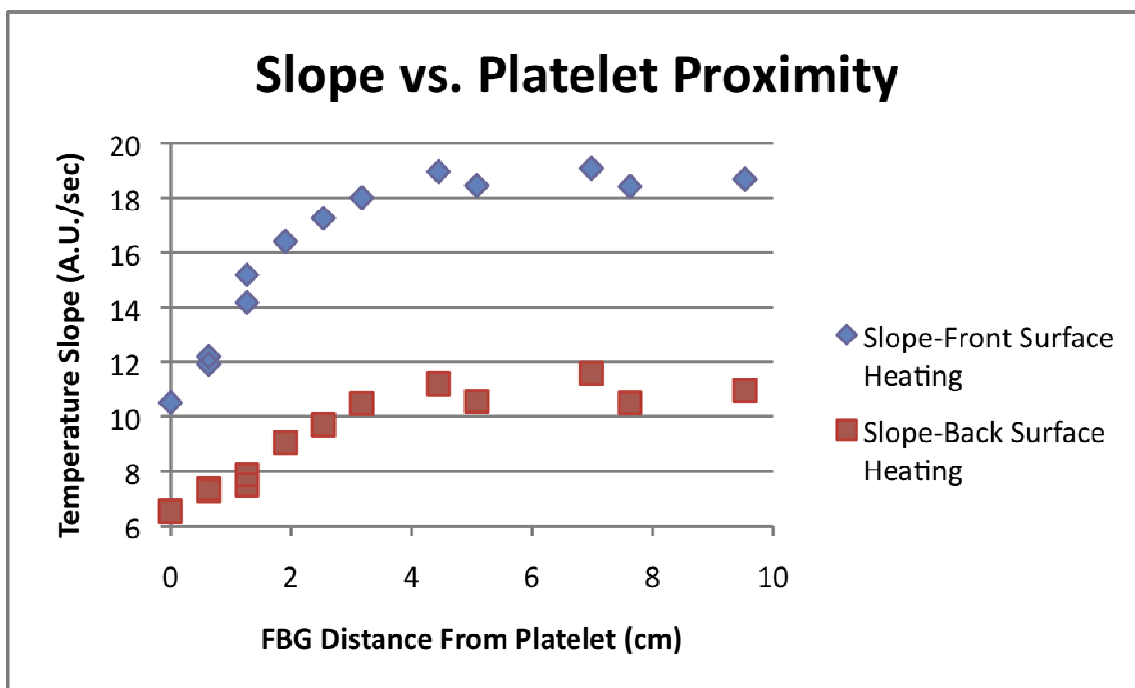

Figure 7. Temperature slopes as determined from linear least-squares fit vs. FBG sensor distance from the center of the nearest heat sink platelet.

As can be seen in Fig. 7, there is a distinct decrease in the rate of temperature increase for FBG sensors in the vicinity of a platelet corresponding to the increase in the effective thickness in the region of a platelet. Since the thickness of the plate relative to the combined thickness of the plate and platelet is 1 to 2.8, then it is expected if the one dimensional model correctly represents the heat flow for this configuration that the rate of temperature change over the platelet should be approximately a third of the rate of temperature change in regions unaffected by the platelet. For the case of heating the surface with the attached fiber optics sensors and the case of heating the opposite surface, the heating rate over the platelet is significantly greater than 1/3 of the heating rate 10 cm from center of the platelet, indicating that the in-plane heat flow in the plate is not negligible. Therefore a two or three dimension model is required to accurately represent the measurements. Also Fig. 7 shows a significant difference between the slopes for front and back surface heating, which disagrees with equations 5 and 6. The significant difference is due to the fact that the front surface was painted black to increase its emissivity, while the back surface was not painted. The painted surface appears to be approximately twice as efficient in absorbing the heat as the untreated surface.
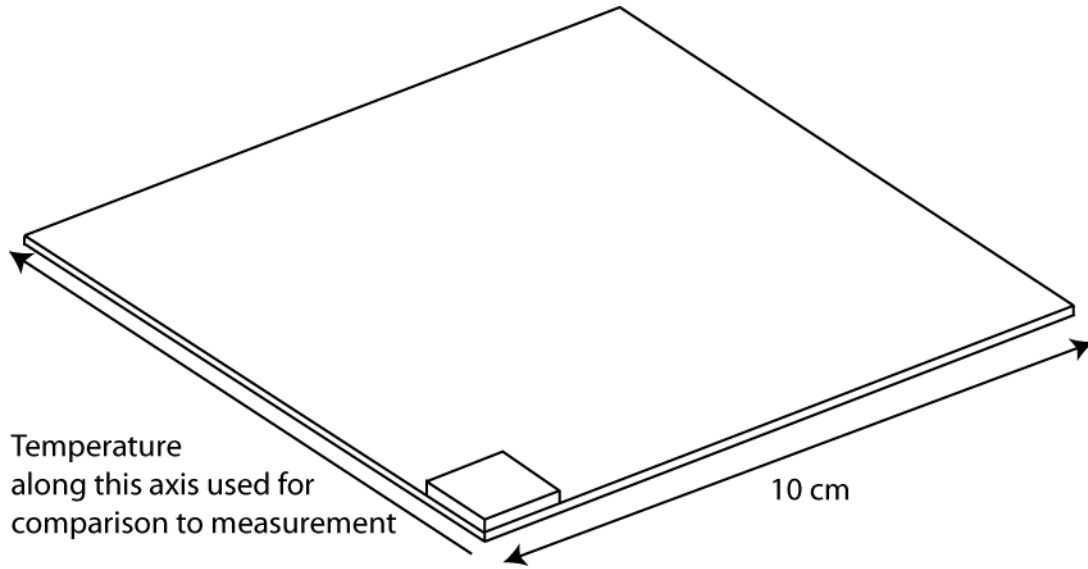

Figure 8. Geometry of FEM simulation of flat plate 20 cm x 20 cm x 0.127 cm with 2.54 cm x 2.54 cm x 0.229 cm platelet in the center. Symmetry allows using simulation geometry of a quarter of the full size (10 cm x 10 cm instead of 20 cm x 20 cm).

5. COMPARISON OF FEM SIMULATIONS AND EXPERIMENTAL RESULTS

To improve the comparison of a thermal model with the measurement, a three dimensional finite element method (FEM) simulation of the plate with attached platelet was developed. The simulation assumes a single platelet attached to the center of a 20 cm x 20 cm x 0.127 cm plate. The size of the platelet was assumed to be 2.54 cm x 2.54 cm x 0.229 cm. Symmetry allows using simulation geometry of a quarter of the full size (10 cm x 10 cm instead of 20 cm x 20 cm) as shown in Fig. 8.

Two simulations were performed, one with the heat flux applied to the surface on the opposite side from the platelet (referred to as front surface heating) and one with the heat flux applied to the exposed surface of the platelet and the surface to which it was attached (referred to as back surface heating). The initial temperature of the total configuration was set to 0. A total of 40 seconds of response was simulated with the heat flux applied for the first 20 seconds. A slight convective loss to an external temperature of 0 degrees was used to simulate the air cooling of the external surface, by setting the heat transfer coefficient to 1 $W/m^2/K$. The nominal values for the properties of steel were used: thermal conductivity 52 W/m/K, density 7850 kg/m^3 and specific heat 475 J/kg/K.
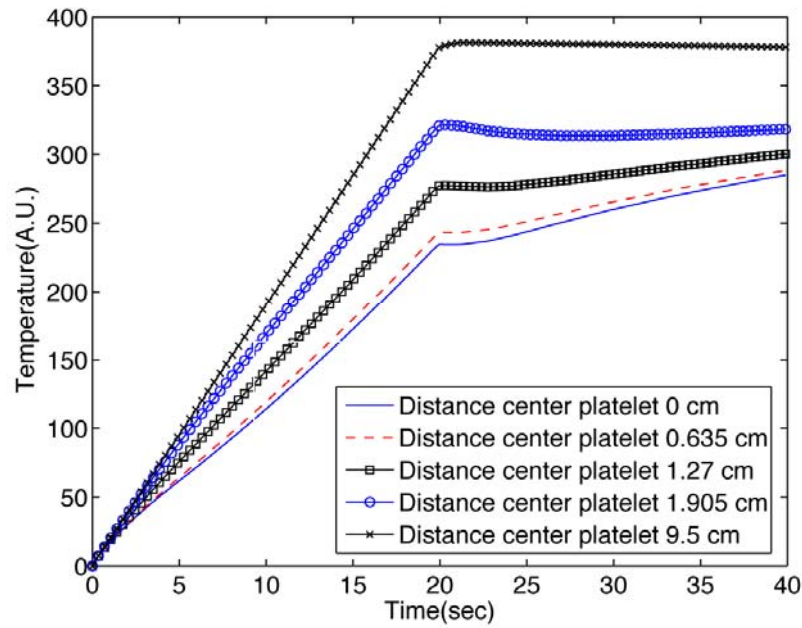
Figure 9. FEM simulation results for front surface heating temperature as a function of time for the same five different positions along axis of object as in Fig. 4.
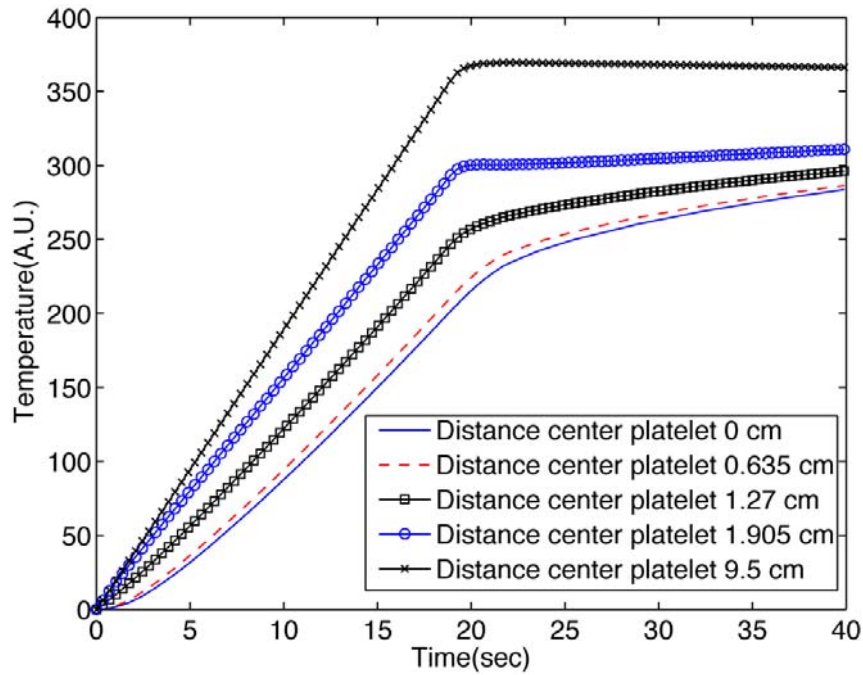

Figure 10. FEM simulation results for back surface heating temperature as a function of time for the same five different positions along axis of object as in Fig. 5.

The time responses for front surface heating at different distances from the center of the platelet are shown in Fig. 9. The temperatures have been scaled to be approximately equal to the measured values for front surface heating. As can be seen from the figure, the responses are similar to those seen in Fig. 4. The rates of heating increase as the distance from the center of the platelet increases, which agrees with the measurement. For points on top of the platelet (less then 1.3 cm), the temperature continues to increase after the heating has turned off, due to in-plane heat flow from the surrounding warmer area to the region of the platelet as is also seen in Fig 4. For the point closest to the platelet (1.905 cm), there is a significantly faster rate of cooling than the point furthest from the platelet (9.5 cm). This indicates that the measurement need not be in a region directly over the platelet, to detect the presence of the platelet.

The time responses for back surface (through transmission) heating at different distances from the center of the platelet are shown in Fig. 10. The temperatures have been scaled to be approximately equal to the measured values. As can be seen from the figure, the responses are similar to those seen in Fig. 5. It is possible to see in both figures that there is a more predominate difference between platelet and no platelet at early times for back surface heating, since the heat must diffuse through the plate and platelet combination before there is an increase in the temperature at the front surface. It is also interesting to note that for both the measured responses and the calculated responses, the transition at the end the heating cycle is smoother as a result of the heat diffusing through the specimen.
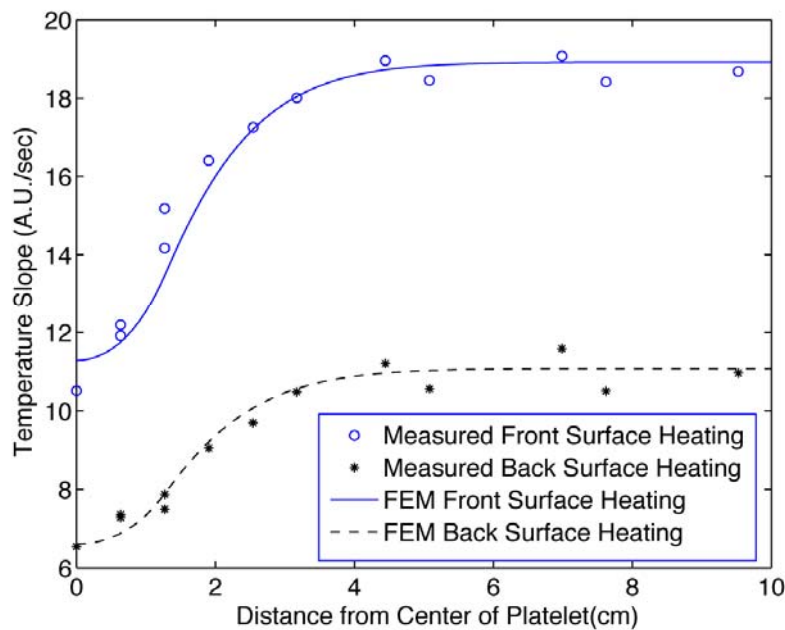

Figure 11. The rate of temperature change during heating cycle based on linear least squares fit of fiber optics measurements and FEM calculations for different distances from the center of the platelet.

A comparison of slopes from the measurement to slopes calculated form the FEM results is shown in Fig. 11. A least squares criterion was used to match the amplitudes for the front surface and back surface heating. After this normalization is performed, there is good agreement between the measurement and FEM slopes. There appears to be a systematic deviation in the 5 measurements furthest from the center of the platelet. This is perhaps indicative of variance in the thermal response of the individual Bragg gratings that could be eliminated by development of an improved calibration technique. From the figure it is possible to see that the slope is significantly impacted by the presence of the platelet at distances from the center of the platelet to approximately its width. This indicates the sensor needs only be in the region of the thickness variation to detect the thermal anomaly caused by the thickness variation.

6. CONCLUSION

A new fiber optic thermography technique previously demonstrated on a composite plate has now been tested on a stainless steel plate to detect thickness variations. The technique uses distibuted FBG sensors for thermographic detection of flaws in materials and structures. Individual fibers with multiple FBGs employed as temperature sensors can be bonded to the surfaces of structures or embedded in the structures. By applying a thermal heat flux to the surface of the investigated structures, the individual Bragg grating sensors successfully measured the temporal and spatial temperature variations on the surface. The thermal responses were consistent with the results from FEM calculations of the thermal response of the specimen. The current research demonstrates capability to detect thickness variations in a 321 stainless steel plate. Good correlation between the measured rate of change of sensor output and the proximity to thickness variations holds promise for corrosion detection. There is also good agreement between the finite element simulation and the measured results. This research demonstrates potential for dual-purpose use of FBG sensors to detect strain as well as corrosion. Future efforts will focus on developing the technique with a faster detection system and assessing its potential for performing thermal health monitoring of aerospace structures and materials.

REFERENCES

1. W. H. Prosser, S. G. Allison, S. E. Woodard, R. A. Wincheski, E. G. Cooper, D. C. Price, A. Tessler and J. L. Spangler, "Structural Health Management for Future Aerospace Vehicles," The Second Australian Workshop on Structural Health Monitoring, Monash University Australia, December 16-17, 2004
2. Prosser, W. H., Wu, M-C, Allison, S. G., DeHaven, S. L. and Ghoshal, A., "Structural Health Monitoring Sensor Development at NASA Langley Research Center," Proceedings of the International Conference on Computational & Experimental Engineering and Sciences (ICCES '03), Corfu, Greece, paper ID 149, July 25-29, 2003.
3. B. A. Childers, M. E. Froggatt, S. G. Allison, T.C.Moore, D.A.Hare, C.F.Batten,, D.C.Jegley,"Use of 3000 Bragg grating strain sensors distributed on four eight-meter optical fibers during static load testing of a composite structure," Proceedings, SPIE's 8th Annual International Symposium on Smart Structures and Materials in Newport Beach, California, Vol. 4332, Paper No. 4332-17, March 2001
4. M. E. Froggatt, and W. Bowen, "Optical Time Domain Reflectometry in Optical Fiber with Reflection Delay Time Matched to the Period of the Optical Frequency Modulation," *Appl. Opt.* , Vol. 37, No. 10, pp. 1731-1734 (1998).
5. M. E. Froggatt and J. Moore, "Distributed Measurement of Static Strain in an Optical Fiber with Multiple Bragg Gratings at Nominally Equal Wavelengths," *Appl. Opt.* , Vol. 37, No. 10, pp. 1741-1746 (1998).
6. M. E. Frogatt, U.S. patent 5,789,521, "Apparatus and Method for Measuring Strain in Bragg Gratings" (1998).
7. T. Brown, K. Wood, B. Childers, R. Cano, B. Jensen, and R. Rogowski; "Fiber Optic Sensors for Health Monitoring of Morphing Aircraft," *Proceedings of The International Society for Optical Engineering (SPIE)*, Vol. 3674, pp. 60-71 (1999).
8. L. Melvin, B. Childers, R. Rogowski, W. Prosser, J. Moore, M. Froggatt, S. Allison, M. C. Wu, J. Bly, C. Aude, C. Bouvier, E. Zisk, E. Enright, Z. Cassadaban, R. Reightler, J. Sirkis, I. Tang, T. Peng, R. Wegreich, R. Garbos, W. Mouyos, D. Aibel, P. Bodan, "Integrated Vehicle Health Monitoring (IVHM) for Aerospace Vehicles," presented at the *International Workshop on Structural Health Monitoring*, Stanford, CA, September 18-20, 1997. In "Structural Health Monitoring Current Status and Perspectives," pp. 705-714, edited by Fu-Kuo Chang, Technomic Publishing Co. Inc., Lancaster, PA, ISBN No. 1-56676-605-2 (1997).

9. M. E. Froggatt, "Distributed Measurement of the Complex Modulation of a Photoinduced Bragg Grating in an Optical Fiber," *Appl. Opt.* , Vol. 35, No. 25, pp. 5162-5164 (1996).
10. A. D. Kersey, M. A. Davis, H. J. Patrick, M. LeBlanc, K. P. Koo, C. G. Askins, M. A. Putnam, E. J. Friebele, "Fiber Grating Sensors," *J. of Lightwave Tech.*, 15(8) (1997).
11. Sidney G. Allison, William H. Prosser, David A. Hare, Thomas C. Moore and W. Scott Kenner, "Optical Fiber Distributed Sensing Structural Health Monitoring (SHM) Strain Measurements Taken During Cryotank Y-Joint Test Article Load Cycling at Liquid Helium Temperatures," proceedings SPIE 6770-2, Boston, MA (2007).
12. M. -C. Wu, W. P. Winfree, and S. G. Allison, "Fiber Optic Thermal Health Monitoring of Aerospace Structures and Materials," Proc. APIE, 729442, 1-9 (2009).
13. S. Gupta, T. Mizunami, T. Yamao, and T. Shimomura, "Fiber Bragg grating cryogenic temperature sensors," Appl. Opt. 25, 5202-5205 (1996).
14. H. S. Carslaw and J. C. Jaeger, Conduction of Heat in Solids, Second Edition, Oxford University Press (1986).
15. "The Mechanical Strength of Silica Optical Fibers," *3M Silica Optical Fibers Application Note* (1995).
16. "The Mechanical and Optical Reliability of Fiber Bragg Gratings," *3M Fiber Bragg Gratings Application Note* (1996).